



Article

## Post-Earthquake Damage and Recovery Assessment Using Nighttime Light Data: A Case Study of the Turkey–Syria Earthquake

Jiaqi Yang, Shengbo Chen \*, Zibo Wang, Yaqi Zhang, Yuqiao Suo, Jinchen Zhu, Menghan Wu, Aonan Zhang and Qiqi Li

College of Geo-Exploration Science and Technology, Jilin University, Changchun 130026, China; jqyang23@mails.jlu.edu.cn (J.Y.); zbwang22@mails.jlu.edu.cn (Z.W.); yaqi23@mails.jlu.edu.cn (Y.Z.); suoyq25@mails.jlu.edu.cn (Y.S.); zjc23@mails.jlu.edu.cn (J.Z.); wumh23@mails.jlu.edu.cn (M.W.); zhangan23@mails.jlu.edu.cn (A.Z.); liqq23@mails.jlu.edu.cn (Q.L.)

\* Correspondence: chensb@jlu.edu.cn

## Highlights

## What are the main findings?

- Damage assessment: This study introduces pixel-level NTL loss to enhance spatially explicit earthquake damage assessment.
- Recovery assessment: This work proposes the Composite Nighttime Light Index (CNLI) to capture recovery dynamics, and develops a Resilience Index (RI) weighted by information gain derived from a Bayesian network to capture resilience levels.

## What is the implication of the main finding?

- Damage assessment: Integrating pixel-level and total NTL loss enhances the precision of identifying severely affected areas.
- Recovery assessment: The combined use of CNLI and RI provides a robust framework for monitoring recovery, assessing resilience, and supporting resilience-oriented planning.

## Abstract

In recent years, the increasing frequency of global seismic events has imposed severe impacts on human society. Timely and accurate assessment of post-earthquake damage and recovery is essential for developing effective emergency response strategies and enhancing urban resilience. This study investigates 11 provinces in Turkey affected by the February 2023 Turkey–Syria earthquake, conducting a multidimensional evaluation of disaster loss and recovery. For loss assessment, existing studies typically focus on changes in the total value of nighttime lights at the regional level, overlooking variations at the pixel scale. In this study, we introduce a pixel-level NTL loss metric, which provides finer-grained insights and helps interpret outcomes driven by spatial heterogeneity. For recovery assessment, we propose a Composite Nighttime Light Index (CNLI) that integrates multiple recovery-phase indicators into a single quantitative measure, thus capturing more information than a one-dimensional metric. To account for complex interrelationships among indicators, a Bayesian network is employed, which moves beyond the conventional independence assumption. Moreover, an information gain (IG) approach is applied to optimize indicator weights, minimizing subjectivity and avoiding abnormal weight distributions compared with traditional methods, thereby ensuring a more objective construction of the Resilience Index (RI). Results show that Sanliurfa, Kilis, and Hatay suffered the most severe damage; Kahramanmaras and Malatya exhibited the lowest CNLI values, while Hatay, Kilis, and Gaziantep showed higher CNLI values. In contrast, Gaziantep and Adana obtained the highest RI values. Since CNLI reflects actual recovery performance while RI



Academic Editor: Fumio Yamazaki

Received: 30 August 2025 Revised: 5 October 2025 Accepted: 13 October 2025 Published: 14 October 2025

Citation: Yang, J.; Chen, S.; Wang, Z.; Zhang, Y.; Suo, Y.; Zhu, J.; Wu, M.; Zhang, A.; Li, Q. Post-Earthquake Damage and Recovery Assessment Using Nighttime Light Data: A Case Study of the Turkey–Syria Earthquake. *Remote Sens.* 2025, 17, 3431. https://doi.org/10.3390/rs17203431

Copyright: © 2025 by the authors. Licensee MDPI, Basel, Switzerland. This article is an open access article distributed under the terms and conditions of the Creative Commons Attribution (CC BY) license (https://creativecommons.org/licenses/by/4.0/).

Remote Sens. 2025, 17, 3431 2 of 22

characterizes inherent resilience, accordingly, effectively linking CNLI and RI establishes a dual-perspective and novel framework, the 11 provinces are classified into four categories, and differentiated recovery strategies are suggested. This study contributes a refined quantitative framework for post-earthquake loss and recovery assessment and provides scientific evidence to support emergency response and targeted reconstruction.

Keywords: nighttime light data; seismic hazard; damage assessment; recovery assessment

## 1. Introduction

In contemporary society, addressing natural disasters has emerged as a pressing global challenge confronting humanity [1], ranking among the most complex and urgent issues of our time. Among various types of natural disasters, earthquakes are particularly frequent and destructive, posing recurrent threats that significantly impede urban development and societal progress [2]. In the context of such critical challenges, the timely and accurate assessment of earthquake-induced damage in the immediate aftermath is essential for effective emergency response and recovery planning [3]. Moreover, subsequent rehabilitation and reconstruction efforts aimed at enhancing urban resilience are essential not only to meet the fundamental survival needs of affected populations but also to ensure the timely and effective delivery of humanitarian assistance [4]. These efforts play a vital role in minimizing long-term disruptions and facilitating the restoration of essential urban functions.

Traditional earthquake damage assessment methods, such as field surveys, are constrained by manpower, time, spatial coverage, and safety. Manual inspections require significant personnel deployment, are time- and resource-intensive, and expose teams to unstable environments and aftershock risks [5], often leading to delays and incomplete coverage, particularly in densely populated or remote areas. UAV-based imaging improves efficiency and safety by remotely acquiring high-resolution imagery, but faces challenges in automation, data consistency, and scalability, as well as constraints from battery life, regulations, weather, and limited range [6,7]. Nighttime light (NTL) remote sensing has emerged as an efficient tool for large-scale, consistent disaster assessment by detecting changes in human activity intensity [8-10], enabling the identification of both abrupt disruptions and gradual recovery patterns [11,12]. Current main NTL sources include DMSP/OLS [13–15] and NPP/VIIRS [16–18], while newer platforms such as SDGSAT-1 [19] and YangWang-1 [20] offer higher resolution but face challenges in data accessibility and continuity. Studies have demonstrated that pre- and post-earthquake NTL variations can delineate affected areas through methods like quadratic difference analysis and significance testing [20], and can reveal socio-economic disruption patterns [21]. Integrating NTL with socio-economic indicators enhances the accuracy of recovery monitoring [22], and strong correlations between NTL changes and physical surface recovery have been observed, such as in the 2015 Nepal earthquake [23]. VIIRS data also support rapid damage-zone identification in emergency response [24]. Despite these advances, existing NTL-based post-earthquake studies have predominantly concentrated on short-term impact detection due to the earthquake, with insufficient attention given to the dynamic, long-term recovery process. It is necessary to integrate approaches that combine damage monitoring with comprehensive recovery evaluation to better support disaster management and reconstruction planning.

NTL remote sensing is not only effective for emergency monitoring but also valuable for tracking urban reconstruction. DMSP/OLS data have been used to reveal macro-level recovery trends after the Wenchuan earthquake (2003–2013) [25], and subsequent studies have linked NTL intensity with economic indicators such as GDP to estimate losses and

Remote Sens. 2025, 17, 3431 3 of 22

infer recovery trajectories [26]. Model-based approaches, such as the post-earthquake NTL segmentation model (PNLP), have further distinguished different recovery stages from emergency response to long-term reconstruction [27]. These findings demonstrate the potential of NTL as an accessible and quantifiable indicator for large-scale recovery monitoring. However, NTL-based outcomes are inherently one-dimensional: lighting recovery does not necessarily represent full recovery across regions or sectors, and similar patterns can arise from non-seismic factors like policy interventions or population relocation [28]. Most existing research remains limited to the visible phenomenon of "lights on," lacking a multidimensional perspective and a comprehensive assessment model that contains multiple dimensions [29]. It is difficult to capture the dynamic complexity of the recovery process, and post-earthquake performance is closely tied to the inherent resilience of cities—something that cannot be fully reflected by nighttime light data alone.

Building on the discussion of NTL remote sensing for disaster monitoring, it is equally important to evaluate the broader resilience of urban systems to fully capture postearthquake recovery dynamics. In recent years, the concept of resilience, which originates from the Latin "resilio," meaning "to return to the original state" [30-32], has been widely applied to disaster risk reduction since its introduction into ecology by Holling [33]. Scholars emphasize that resilience assessment should address the ability not only to withstand disasters but also to recover and adapt rapidly after events such as earthquakes [34–36]. Common approaches involve constructing index systems or computational models, with weighting methods evolving from Analytic Hierarchy Process (AHP), expert scoring, and entropy weighting to integrated techniques such as TOPSIS [37] and ISM-ANP-TOPSIS [38] for evaluating vulnerability in terms of exposure, sensitivity, and response capacity [39]. Recent advances combine fuzzy set theory with Geographic Information Systems (GIS) for spatial visualization [40-42], and emerging studies have introduced machine learning and cluster analysis to enhance evaluation accuracy [43]. Despite these developments, existing methods still face issues such as expert opinion in subjective weighting, limited relational modeling in objective weighting, and sensitivity to data variability. Moreover, they struggle to capture complex, non-linear relationships among indicators [44–46]. In contrast, machine learning, though still emerging in this field, offers advantages in data-driven analysis and pattern recognition [47]. This study leverages machine learning to objectively determine indicator weights, thereby mitigating the impact of data variance for enhanced accuracy in seismic resilience assessment.

Against this backdrop, this study utilizes NTL data for post-disaster loss and recovery assessment. For damage assessment, earthquake impacts are quantified using a set of indicators derived from NTL. For recovery assessment, a Composite Nighttime Light Index (CNLI) is developed, and a Bayesian network is employed to model the interrelationships among resilience indicators and recalculate their weights using the machine learning method. Based on this framework, the relationship between CNLI and the resilience index (RI) is analyzed, and affected areas are classified into four levels. This integrated approach supports timely disaster assessment and provides a reference for post-disaster decision-making.

## 2. Study Area and Datasets

## 2.1. Study Area

This study focuses on the 2023 Turkey–Syria earthquake, one of the largest recorded continental strike-slip earthquakes in the modern instrumental era [48]. On 6 February 2023, a devastating earthquake with a moment magnitude (Mw) of 7.8 struck near Kahramanmaraş, severely impacting southeastern Turkey and northern Syria. The event occurred at 04:17:34 local time, lasted for approximately 90 s, and produced a surface rupture ex-

Remote Sens. 2025, 17, 3431 4 of 22

tending about 380 km. Roughly nine hours later, another major earthquake with Mw 7.5 occurred along an independent fault located about 100 km north of the first epicenter, generating a surface rupture of about 200 km. Together, these twin events represent the largest recorded continental doublet earthquakes since the advent of modern seismic instrumentation. Within a single day, several earthquakes exceeding Mw 7.0 struck the region, resulting in over 50,000 fatalities, more than 100,000 injuries, and rendering more than half a million buildings uninhabitable.

The earthquakes were driven by westward motion along the East Anatolian Fault Zone (EAFZ), one of the most seismically active regions in Turkey, which extends for about 580 km and has historically generated multiple large events [49]. It serves as a boundary fault between the Anatolian Plate and the Arabian Plate, connecting to the Dead Sea Fault (DSF) at its southwestern end [50].

The study area covers southeastern Turkey, encompassing eleven provincial administrations and more than twenty county-level areas (Figure 1). The selected area in the figure corresponds to the surface rupture zone generated by the earthquake. These areas have been affected to varying degrees, with the most severe impacts observed in Hatay, Kahramanmaraş, and Gaziantep.

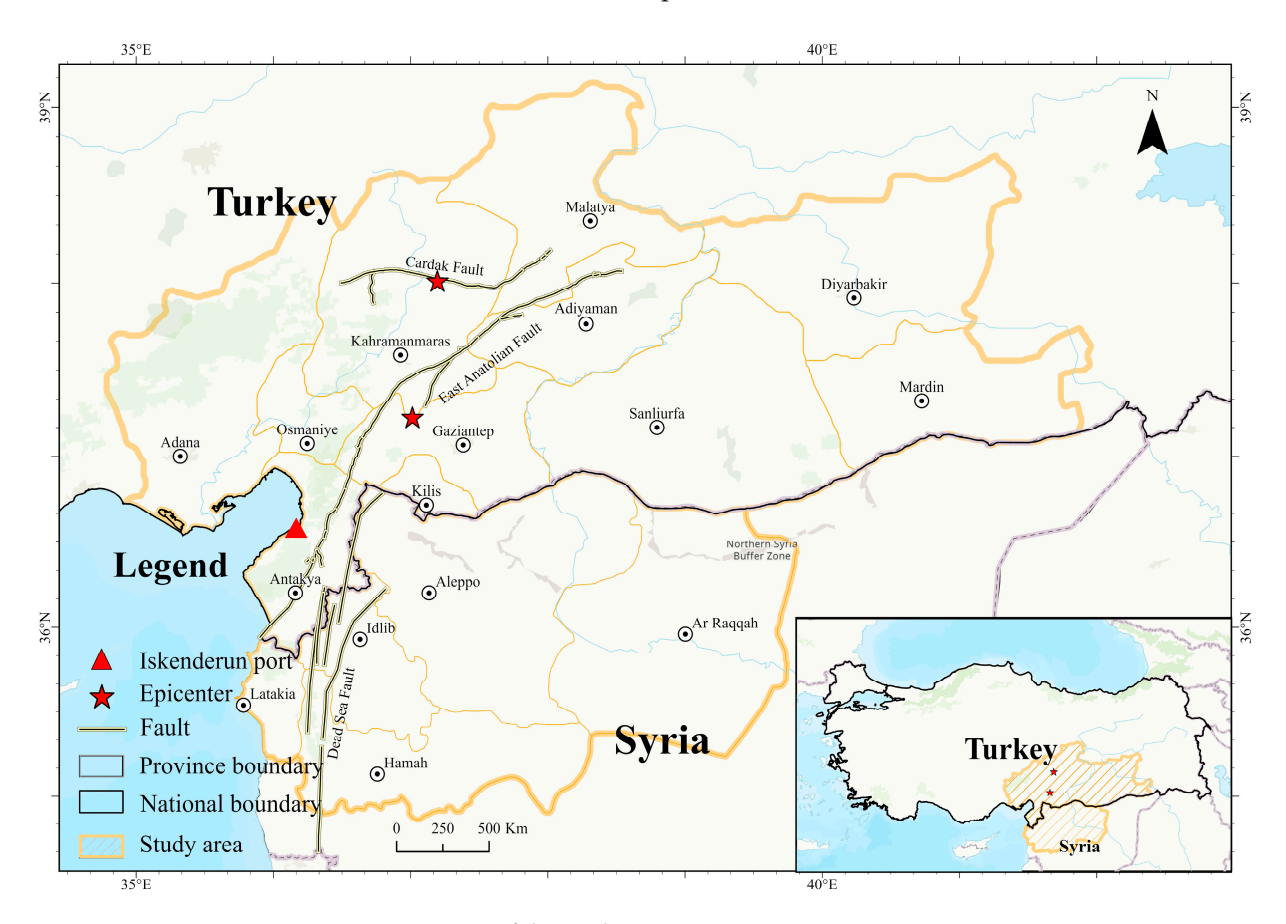


Figure 1. Location of the study area.

#### 2.2. Datasets

#### (1) Daily NTL Data

Due to variability in available data, this study adopted the NPP/VIIRS Black Marble VNP46A2 product, which is well-suited for rapid response and large-scale hazard assessment. Compared with DMSP/OLS, VIIRS offers higher spatial resolution and improved radiometric calibration, enabling more accurate monitoring of artificial nocturnal lighting [51,52]. The data have a spatial resolution of 15 arcseconds with daily temporal coverage, comprising seven

Remote Sens. 2025, 17, 3431 5 of 22

data layers [53]. We used the Gap Filled DNB BRDF Corrected NTL layer, which fills missing values with the most recent high-quality data and applies corrections for clouds, atmosphere, topography, vegetation, snow, moonlight, and stray light.

## (2) Monthly NTL Data

This study also employs the monthly NPP-VIIRS NTL product, available since April 2012 and updated regularly. Two formats are provided: "vcm" (VIIRS Cloud Mask) and "vcmsl" (VIIRS Cloud Mask with Stray Light correction), covering  $65^{\circ}$ S– $75^{\circ}$ N at a resolution of  $86,401 \times 33,601$  pixels [52,54]. As "vcm" data for January–December 2023 are incomplete in the study area, the "vcmslfg" version was selected for its higher quality and spatial completeness. With moderate spatial resolution and high temporal frequency, this dataset is well-suited for diverse Earth observation applications.

#### (3) Statistics of Turkey

Urban statistical data were obtained from the Turkish Statistical Institute (TURKSTAT). The dataset includes eight indicators: Total number of hospitals (f1), Total number of physicians (f2), Road length (f3), Electricity consumption (f4), Population (f5), Per capita GDP (f6), Total built-up area (f7), and Proportion of population served by wastewater treatment (f8). The analysis uses 2022 data at the provincial level.

## (4) Auxiliary Data

Land cover data for 2022 were obtained from the Land Cover Explorer on the ArcGIS platform. From the ten land cover categories, Vegetation and Rangeland were extracted to represent the Proportion of green space (f9), later used in calculating indicator weights for the seismic resilience model. Provincial boundary data were sourced from the Global Administrative Areas database (GADM).

#### 3. Method

The experimental workflow of this study is illustrated in Figure 2. First, NPP/VIIRS NTL data, statistical data of Turkey, and auxiliary datasets are collected. Preprocessing steps are applied to the NTL data, including outlier removal and projection transformation. In parallel, statistical and auxiliary data are calculated and normalized. In terms of damage assessment, four NTL indicators are selected using daily products to evaluate post-earthquake losses. In terms of recovery assessment, monthly data are used to construct CNLI indicators, and a multi-indicator resilience assessment model composed of statistical data and land cover data is established. The index relationship is characterized by the Bayesian network, and the RI is calculated separately for each city by relying on the IG method. Further, the regional categories are reclassified by combining the two. A comprehensive assessment of post-earthquake losses and recovery is achieved through the above content.

#### 3.1. Data Pre-Processing

Due to data availability and temporal continuity constraints, the NPP/VIIRS VNP46A2 product was selected, with 30 January 2023, as the pre-disaster date and 8 February 2023, as the post-disaster date. These datasets were cropped, masked, cleaned of outliers, and processed with Kriging interpolation for damage evaluation (in Table 1). Monthly NTL data from January to December 2023 were also used, with preprocessing steps including removal of negative values, cropping, projection transformation, and resampling to improve NTL index accuracy.

Remote Sens. 2025, 17, 3431 6 of 22

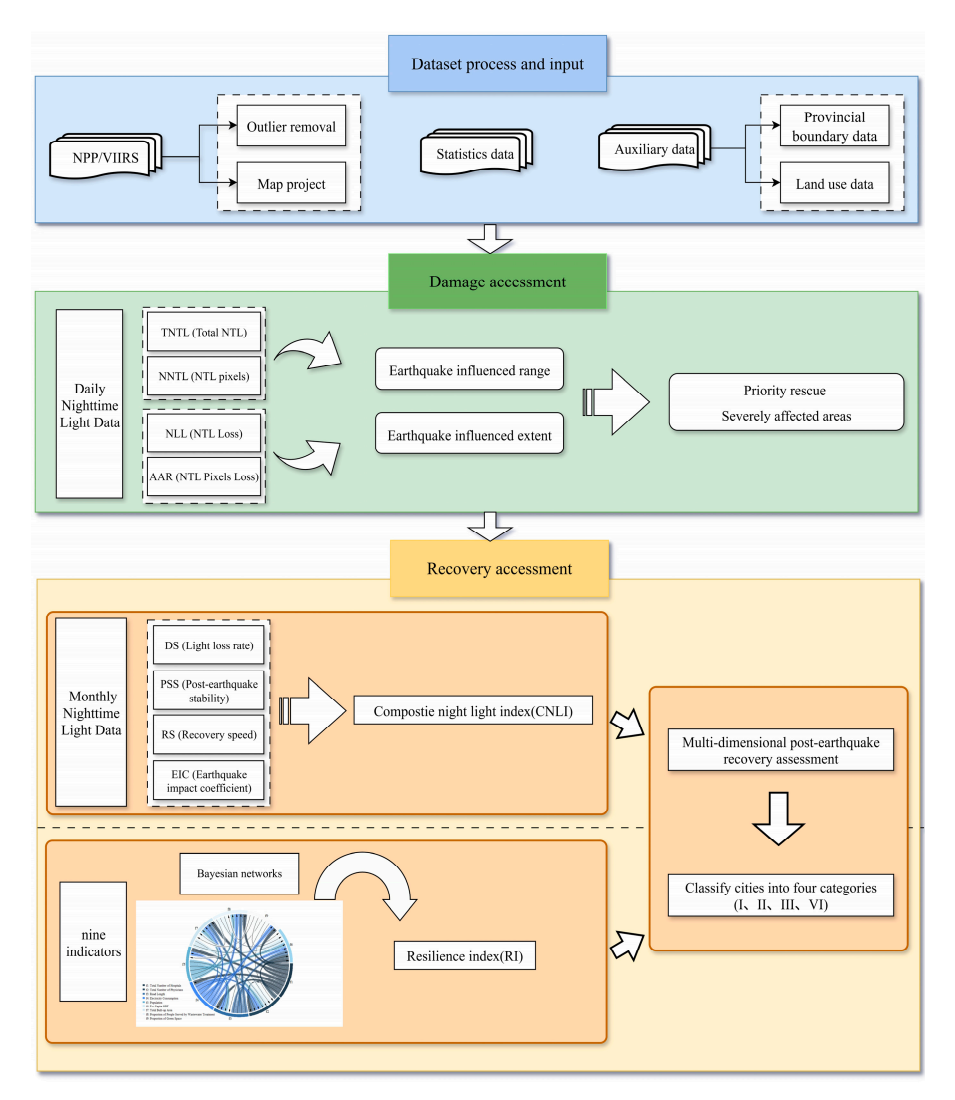


Figure 2. Flowchart of post-earthquake damage and recovery assessment using NTL data.

Table 1. Data Instructions.

Assessment Phase	Data Instructions		
Damage Assessment	Pre-earthquake Date: 31 January 2023; Post-earthquake Date: 8 February 2023		
Recovery Assessment	Monthly NTL Data: January 2023–December 2023		

Land cover data were reclassified into nine categories, from which vegetation and flooded vegetation were extracted to calculate the green land coverage ratio (f9) as an ecological indicator in Equation (1):

$$f9 = \frac{Area_{greenland}}{Area_{all}} \tag{1}$$

where  $Area_{greenland}$  is the calculated greenland area, and  $Area_{all}$  is the area of all categories of land in each area.

#### 3.2. NTL Metrics for Quantitative Earthquake Damage Assessment

In this study, the Total nighttime light index (*TNTL*) and the number of nighttime light pixels (*NNTL*) are selected as indicators for assessing earthquake-related losses. The TNLI calculation formula is provided in Equation (2).

Remote Sens. 2025, 17, 3431 7 of 22

$$TNTL = \sum_{i=1}^{b} D N_i \tag{2}$$

where b is the number of rasters and D  $N_i$  is the radiant value of the image element corresponding to each raster.

Meanwhile, the Number of Nighttime Light pixels (*NNTL*) represents the number of NTL image pixels [18], where only pixels with brightness values greater than zero are included. The calculation is shown in Equation (3).

$$NNTL = \sum_{i=1}^{N} L_i \cdot II(L_i > 0)$$
(3)

where NNTL is the total number of non-zero NTL pixels, and N is the total number of raster pixels.  $L_i$  denotes the NTL value of the ith pixel. The indicator function II ( $L_i > 0$ ) is an indicator function that ensures that only pixels with luminance greater than 0 are accrued.

To further quantify the seismic impact, Nighttime light loss (*NLL*) is introduced to reveal the overall extent of the current earthquake's impact on human activity areas and power supply. The *NLL* is calculated by using Equation (4).

$$NLL = \frac{\sum L_{pre} - \sum L_{post}}{\sum L_{pre}}$$
 (4)

where  $\sum L_{pre}$  and  $\sum L_{post}$  denote the sum of TNL before and after the earthquake, respectively. NLL value denotes the proportion of NTL loss in the range [0, 1].

In addition, the proportion of change in NTL imagery is calculated to obtain the Area affected by the earthquake (*AAR*), as defined in Equation (5). The *AAR* is employed to assess the extent of earthquake damage to human settlements and power supply infrastructure.

$$AAR = \frac{N_{pre} - N_{post}}{N_{pre}} \tag{5}$$

where  $N_{\text{pre}}$  and  $N_{\text{post}}$  denote NNTL before the earthquake and NNTL after the earthquake.

## 3.3. Recovery Assessment Methods

## 3.3.1. Development of the Composite Night Light Index (CNLI) for Recovery Assessment

This study employs monthly NTL data from January to December 2023 to quantify post-earthquake human activity recovery. In February (earthquake month), TNTL increases due to intensive rescue efforts, while March records the lowest values as infrastructure remains unrepaired. April–December marks the recovery phase, assessed using the light loss rate (DS), recovery speed (RS), post-seismic stability (PSS), and earthquake impact coefficient (EIC).

The light loss rate (DS) quantifies the degree of decline in human activity caused by the earthquake, and its calculation method is shown in Equation (6).

$$DS = \frac{MarchNTL - FebNTL}{FebNTL} \tag{6}$$

where *MarchNTL* and *FebNTL* are the regional TNTL values in March and February, respectively.

Recovery Speed (RS) denotes the period from the darkest point of the post-earthquake (March) to the initial recovery stage (June), and the statistical method is as in Equation (7).

$$RS = \frac{JuneNTL - MarchNTL}{JanNTL - MarchNTL} \tag{7}$$

where JuneNTL and MarchNTL are the regional TNTL in June and March, respectively.

Remote Sens. 2025, 17, 3431 8 of 22

Post-Seismic Stability (PSS) measures whether the region stabilizes after the earthquake by the light fluctuation coefficient from April to December, and the statistical method is shown in Equation (8).

$$PSS = \sqrt{\frac{1}{n} \sum_{t=4}^{12} \left( PSS_t - P\overline{S}S \right)^2}$$
 (8)

where  $PSS_t$  and  $P\overline{S}S$  are the TNTL value and average NTL value of the month, respectively. Earthquake Impact Coefficient (EIC) is used to regulate the variability of different regions in the degree of damage [55]. It is expressed in normalized form. The calculation follows Equations (9) and (10).

$$d = 2R \times \arcsin\left(\sqrt{\sin^2\left(\frac{\Delta\phi}{2}\right) + \cos\phi_1\cos\phi_2\sin^2\left(\frac{\Delta\lambda}{2}\right)}\right)$$
 (9)

where R is the radius of the Earth,  $\phi$  is the latitude, and  $\lambda$  is the longitude.

$$EIC = \frac{1}{d_i} \tag{10}$$

where  $d_i$  denotes the actual distance of each region to the epicenter.

The Composite NTL Scoring Model is fitted to calculate the Composite Night Light Index (CNLI) of each region and sorted as in Equation (11).

$$CNLI = A_1 \times RS + A_2 \times (1 - DS \times EIC) + A_3 \times \left(1 - \frac{PSS}{\max(PSS)}\right)$$
(11)

where DS denotes the rate of light loss, RS denotes the rate of recovery, PSS denotes the post-earthquake stability, EIC denotes the coefficient of seismic influence, and the three constant coefficients of  $A_1$ ,  $A_2$ , and  $A_3$  are jointly determined by the least squares fitting method of the regression model and the expert scoring method. It measures the contribution of the rate of recovery of the initial loss and the long-term stability to the comprehensive post-earthquake NTL performance, respectively.

# 3.3.2. Development of a Bayesian Network–Based Information Gain Method for Recovery Assessment

This study introduces an information gain (IG) method based on Bayesian networks to learn both structure and weights in a data-driven manner, enabling interpretable modeling and accurate identification of key post-disaster recovery factors. First, taking statistical data and land cover data as input, Bayesian networks represent conditional dependencies among variables as a Directed Acyclic Graph (DAG). Structure learning is performed using the Hill-Climbing algorithm with the K2 scoring function [56]. The K2 scoring function takes the form of Equation (12). The network structure may change with the initial order of the nodes.

$$K2(G|D) = \prod_{i=1}^{n} \prod_{j=1}^{q_i} \frac{(r_i - 1)!}{(N_{ij} + r_i - 1)!} \prod_{k=1}^{r} N_{ijk}!$$
 (12)

where G denotes the network structure, D denotes the observed dataset, n is the number of variables,  $q_i$  is the number of parent node combinations of the ith node,  $r_i$  is the number of its possible values, and  $N_{ijk}$  is the number of samples when the node i takes the kth value and the combination of its parent nodes is the jth one.

On this basis, Information gain [57] quantifies each indicator's ability to reduce the uncertainty of the resilience index (RI), as in Equation (13).

$$IG(Y, X_i) = H(Y) - H(Y|X_i)$$
(13)

Remote Sens. 2025, 17, 3431 9 of 22

where H(Y) represents the entropy of the RI, and  $H(Y|X_i)$  denotes the conditional entropy in the case of the given variable  $X_i$ . The greater the information gain, the more the variable can reduce the uncertainty of the results, and the higher its weight, the more significant its influence on the toughness results, according to which the new weight values of the indicators in the seismic toughness assessment model are set.

By normalizing the IG values of all indicators, the weight of each indicator is obtained. By calculating the IG for all indicators and normalizing them to obtain the weight  $w_i$ , the calculation is shown in Equation (14).

$$w_{i} = \frac{IG(Y, X_{i})}{\sum_{j=1}^{n} IG(Y, X_{j})}$$
(14)

where  $w_i$  denotes the weight of indicator i,  $IG(Y, X_i)$  represents the information gain between Y and  $X_i$ , and the denominator is the total information gain from all indicators.

Finally, the normalized value of each indicator  $X_i$  and the corresponding weight  $w_i$  are weighted and summed to calculate the urban seismic RI, which is calculated as shown in Equation (15).

$$RI = \sum_{i=1}^{9} w_i \cdot x_{i,norm} \tag{15}$$

where  $x_{i,norm}$ : the normalized value of the i th indicator,  $w_i$ : the information gain weight of the ith indicator. The comprehensive RI can reflect the overall seismic resilience of the region under the multidimensional system and provide scientific reference for urban planning and post-disaster reconstruction.

In the modeling of the RI, a total of nine indicators (f1–f9) were selected based on historical earthquake cases and influencing factors reported in related studies [33], as well as the types of data publicly released by the Turkish Statistical Institute.

#### 4. Result

## 4.1. Damage Quantitative Assessment Result

The TNTL values, the NNTL, the NLL, and the losses in AAR within the study area were calculated at the provincial scale to visualize changes in the TNTL before and after the earthquake, as shown in Figure 3. Moreover, in Syria, five regions are severely affected [17], with Aleppo in particular suffering major losses, highlighting the destructive impact of the earthquake beyond Turkey's borders.

In this study, eleven provincial administrations in Turkey affected by the earthquake were selected to calculate pre-earthquake and post-earthquake changes in TNTL and the NTL pixels to assess the extent of the damage. The specific calculation results are presented in Figure 4. The largest TNTL losses occurred in Sanliurfa, Kilis, Hatay, and Gaziantep, with losses of 28.80%, 19.63%, 16.78%, and 16.80%, respectively, findings that are consistent with those reported [17]. Additionally, analysis of NTL pixel losses revealed that Sanliurfa, Hatay, Adiyaman, and Mardin experienced the greatest percentage losses, reaching 41.73%, 19.76%, 19.66%, and 19.28%, respectively. The NLL and AAR show a relatively similar changing trend, indicating not only a decrease in value but also the disappearance of pixel brightness, such as in Sanliurfa. Although the overall NLL in Hatay is not the highest, the AAR is relatively prominent. Combined with the analysis in Figure 3c,e. Perhaps the Iskenderun port remained relatively stable, but the vast other areas suffered extremely thorough damage. Pixel-level indicators better reflect this internal imbalance, highlighting the heterogeneity destruction pattern of disasters.

Remote Sens. 2025, 17, 3431 10 of 22

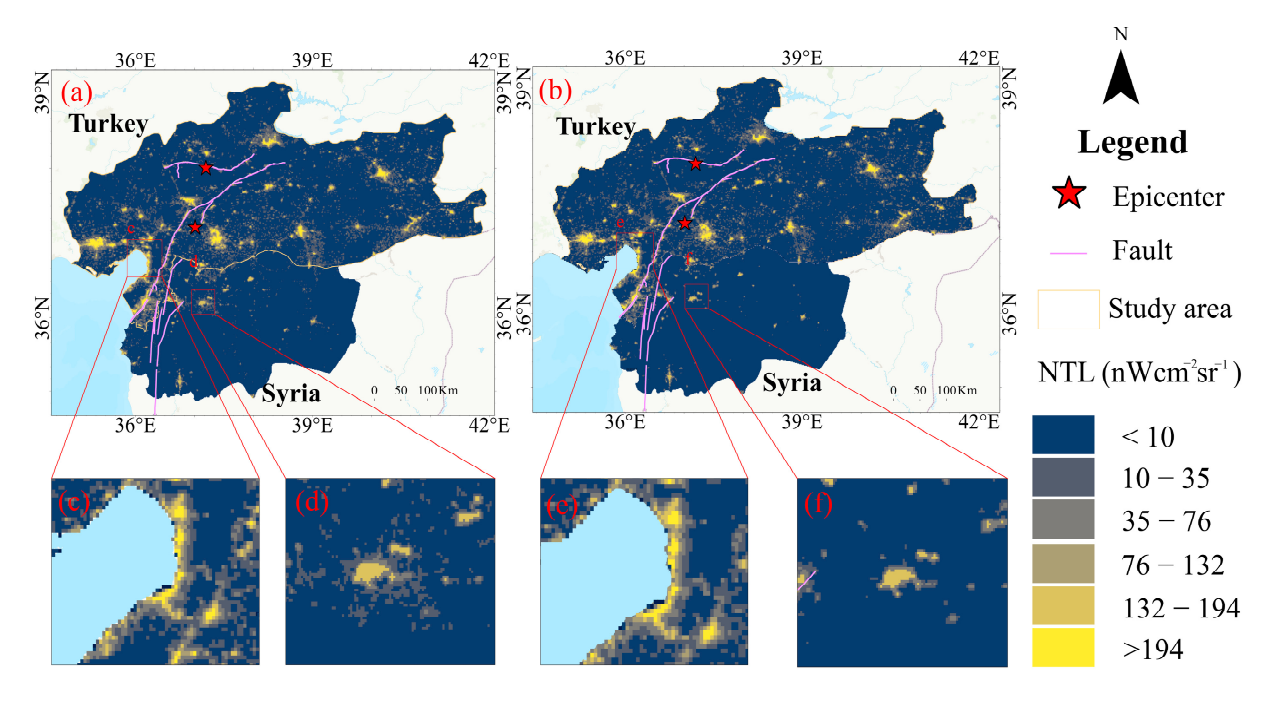


**Figure 3.** Comparison of NTL in the study area before (a) and after the earthquake (b). (c,e) are the NTL conditions before and after the Hatay earthquake, respectively, and (d,f) are the NTL conditions before and after the Aleppo earthquake, respectively.

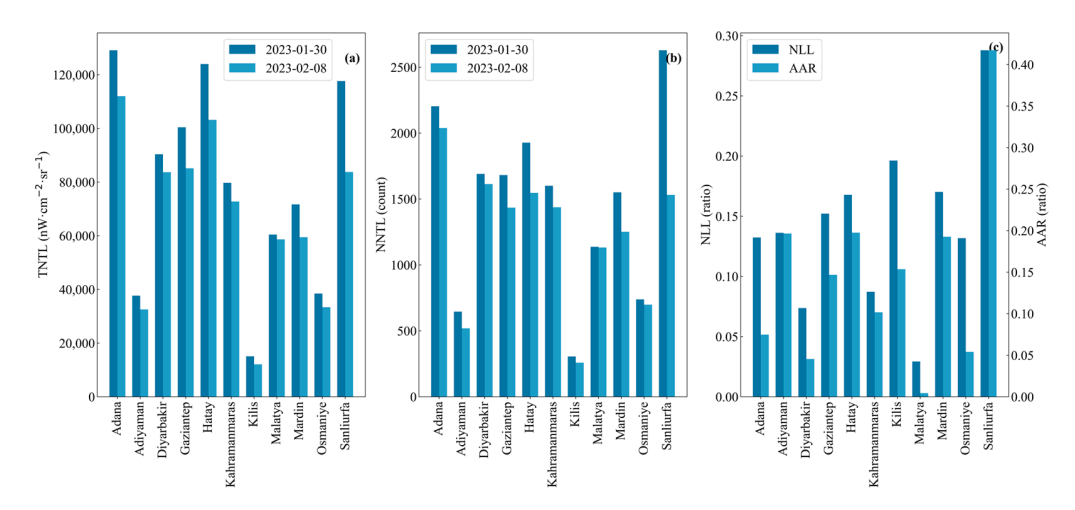


**Figure 4.** The maps of TNTL (a), NNTL (b), NLL and AAR (c) in the study area. The blue legends represent the data before the earthquake, and the light blue legends represent the data after the earthquake.

There is the same trend of the loss of the two metrics, where the degree of loss of both metrics is higher in Sanliurfa, followed by Mardin and Hatay (Figure 4).

## 4.2. CNLI for Recovery Quantitative Assessment

The DS results indicate that most regions experienced post-earthquake NTL attenuation, except Hatay, where values slightly increased. According to the World Bank Group's Loss Assessment Report [58], Hatay suffered severe damage (36% total loss, ~40% capital stock loss), leading to a sharp TNLI drop followed by gradual recovery. Malatya and Kahramanmaras recorded the highest light loss rates (32.9% and 22.2%), consistent with their proximity to the epicenters. RS values were highest in Hatay, Kahramanmaras, and Sanliurfa (>1.28), indicating strong recovery momentum despite severe damage. PSS values revealed higher volatility in Malatya, Sanliurfa, and Diyarbakir, reflecting unstable recovery. CNLI rankings

Remote Sens. 2025, 17, 3431 11 of 22

show Hatay (0.88) and Gaziantep (0.82) with the best long-term performance, while Malatya had the lowest RS (0.048) and PSS, signifying weak recovery (Table 2).

Table 2. The values of various indicators, the comprehensive NTL index and their rankings in each
region after the earthquake.

Region Name	DS	RS	PSS	EIC	CNLI	CNLI Sort
Hatay	+0.028	1.357	9800	0.40	0.88	1
Gaziantep	-0.044	0.007	6200	0.72	0.82	2
Kilis	-0.161	0.902	1200	0.75	0.85	3
Osmaniye	-0.163	0.969	3000	0.38	0.78	4
Adana	-0.109	0.208	7500	0.45	0.75	5
Sanliurfa	-0.120	1.380	16,000	0.65	0.72	6
Adiyaman	-0.133	0.843	4000	0.80	0.70	7
Diyarbakir	-0.142	0.892	12,000	0.55	0.68	8
Kahramanmaras	-0.222	1.280	6500	0.95	0.65	9
Mardin	-0.160	0.683	9800	0.35	0.60	10
Malatya	-0.329	0.048	15,000	0.90	0.35	11

Cities were categorized into three groups according to EIC values: High (>0.7), Medium (0.5–0.7), and Low (<0.5). There were clear differences across groups (Figure 5), as DS tends to decrease as EIC increases, with the High-EIC group showing more negative values and wider variability; RS exhibits relatively stable values in the Medium-EIC group, while the High-EIC group displays a broader range, reflecting divergent recovery dynamics; and the PSS value was at the leading level in the Medium-EIC group, indicating stronger spatial heterogeneity of damage, which is consistent with the "transition zone effect" [59] often discussed in earthquake engineering. In contrast, the high-EIC group exhibits relatively lower PSS values, but with a more scattered distribution.

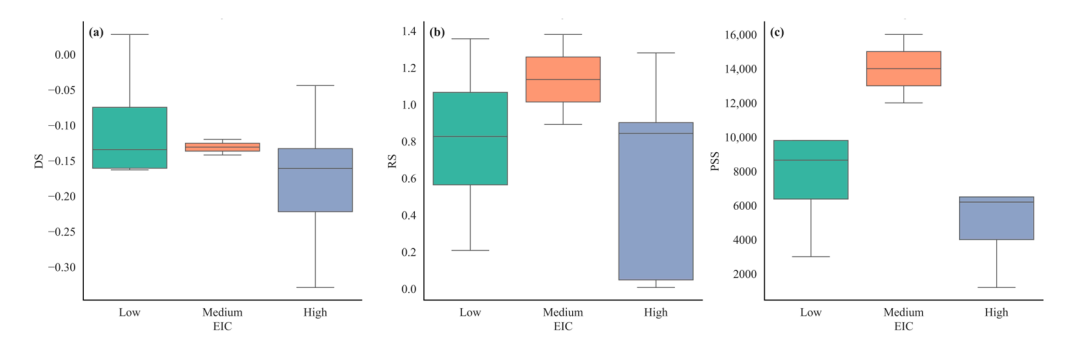


**Figure 5.** Box plots of urban DS, RS and PSS grouped by seismic impact factor (EIC). The DS distribution (a), RS distribution (b) and PSS distribution (c) of the low, medium and high EIC groups.

#### 4.3. Recovery Quantitative Assessment Result

#### 4.3.1. The Relationship Between Indicators

Based on the results obtained from NTL performance, the urban earthquake resilience is further examined. In this study, the stability of the network structure was verified by repeatedly altering the initial ordering of nodes. Across multiple experimental repetitions, the resulting network structure remained entirely consistent rather than being dependent on specific initial conditions, thereby enhancing the generalizability of the proposed framework. The complex dependency relationships among the indicators are first determined using a Bayesian network, as illustrated in Figure 6. In the network, an arrow points from a parent node to a child node, indicating that the parent node influences the child node and that a dependency relationship exists between them. From Figure 6, it is evident that population occupies a central position in the network, directly affecting key variables such as Total Built-up Area, Total Number of Hospitals and Per Capita GDP, thereby reflecting its role as a core carrier. Per Capita GDP is influenced not only by infrastructure variables,

Remote Sens. 2025, 17, 3431

including hospitals and building area, but also by the number of physicians, indicating a bidirectional linkage between the level of economic development and basic service capacity. The relationship between road length and the proportion of the population served by wastewater systems demonstrates the coupling between infrastructure components. Meanwhile, the correlations between green space area and multiple variables indicate that the utilization of ecological space is a key factor shaping the region's functional structure.

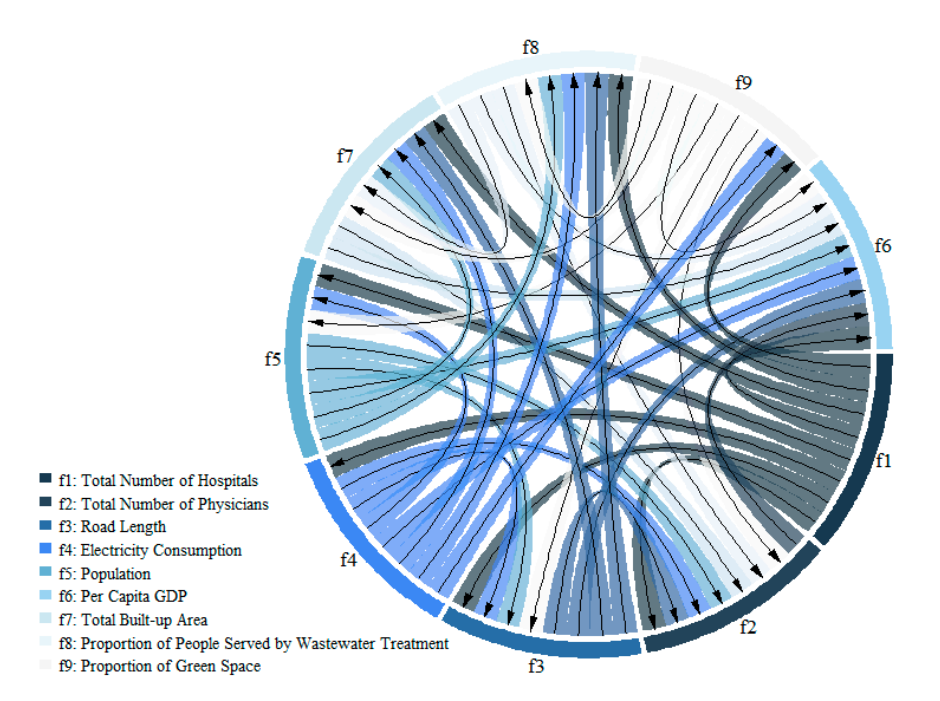


**Figure 6.** Bayesian networks describe the complex relationships among indicators across dimensions, where the arrows indicate parent–child influence, and the arrows from a to b indicate that a has a direct influence on b.

#### 4.3.2. Obtain More Objective Weights Through the IG Method

The indicator system, comprising statistical and land cover data from eleven provincial regions identified as disaster-affected areas in Turkey, was re-weighted using the IG method. Nine indicators were selected and visualized in the plotting diagram. Figure 7 presents the normalized interaction values of the weights for each indicator across the regions. Based on the distribution of the original data, Gaziantep and Adana perform well across all indicators, while Kilis and Adiyaman perform slightly worse.

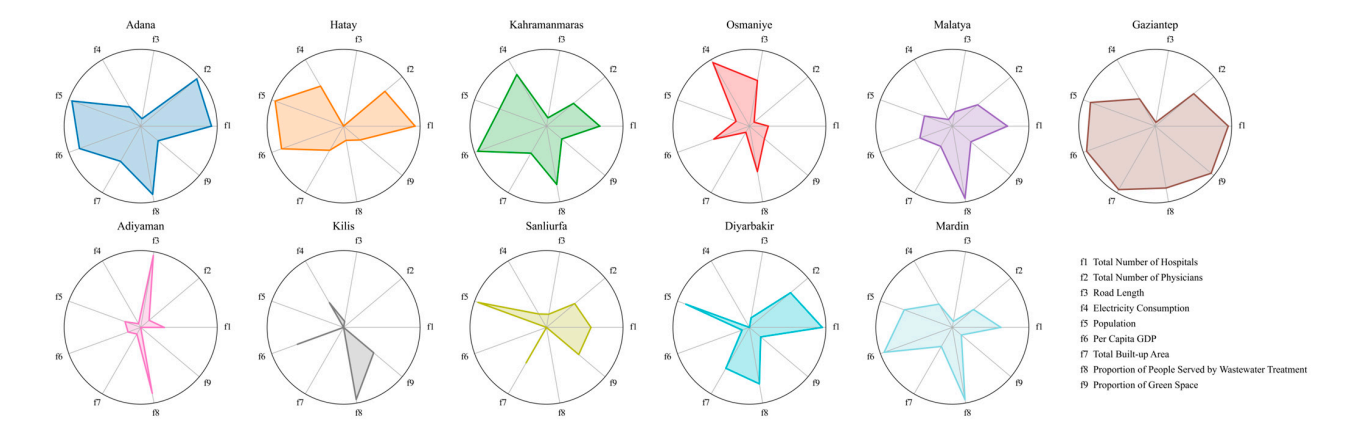


**Figure 7.** Interactive heatmap of regions and indicators. This figure illustrates the distribution of standardized indicator values for eleven earthquake-affected regions in southeastern Turkey.

Remote Sens. 2025, 17, 3431

The weight values of the nine indicators used in assessing seismic urban resilience, calculated using the IG method based on the Bayesian network, are presented in Table 3. Population (0.1378), Total Number of Hospitals (0.1339), Total Built-up Area (0.1330), and Per Capita GDP (0.1281) have the highest weights, indicating their significant influence on the comprehensive resilience assessment and forming a foundation for the subsequent calculation of the RI.

Indicator	Weight Value
Total Number of Hospitals	0.1339
Total Number of Physicians	0.1223
Road Length	0.0610
Electricity Consumption	0.1117
Population	0.1378
Per Capita GDP	0.1281
Total Built-up Area	0.1330
Proportion of People Served by Wastewater Treatment	0.0869
Proportion of Green Space	0.0854

## 4.3.3. RI and Spatial Distribution in Each Region

To visualize the degree and spatial distribution of urban earthquake resilience, the RI for each region was calculated and ranked, as shown in Table 4. Gaziantep and Adana rank at the top, while Kilis and Adiyaman are positioned toward the lower end. The distribution presented in Figure 8 corroborates these findings. Notably, Mardin ranks the lowest, reflecting the compounded effects of multiple dimensions of vulnerability.

Table 4. Urban earthquake RI, ranking and grade of each region.

Region Name	RI	RI Sort	Туре
Gaziantep	0.8201	1	Resilient
Adana	0.7256	2	Resilient
Hatay	0.4626	3	Vulnerable
Diyarbakir	0.4574	4	Vulnerable
Kahramanmaras	0.4438	5	Vulnerable
Sanliurfa	0.4185	6	Vulnerable
Osmaniye	0.3784	7	Vulnerable
Malatya	0.3497	8	Sluggish
Adiyaman	0.2776	9	Sluggish
Kilis	0.2680	10	Sluggish
Mardin	0.2649	11	Sluggish

Among all the indicators, the weight of healthcare resources is particularly significant. In Adana, Gaziantep, and Diyarbakir, the indicator curves for Total Number of Hospitals and Total Number of Physicians peak prominently, indicating that the robustness of the healthcare system is a key factor supporting higher resilience levels. This finding is consistent with previous research highlighting the pivotal role of healthcare infrastructure in effectively responding to sudden-onset disasters [60]. The influence of transportation and infrastructure varies by region. Osmaniye and Kilis exhibit high values for Road Length and Electricity Consumption, reflecting a greater reliance on transport and infrastructure systems for resilience. In contrast, Malatya and Mardin display relatively flat indicator curves, suggesting underdeveloped infrastructure, which negatively impacts their overall resilience levels. Population and economic capacity are major contributors to resilience.

Remote Sens. 2025, 17, 3431 14 of 22

Adana, Gaziantep, and Sanliurfa exhibit higher weights for the Population and Per Capita GDP dimensions, proving that economic vitality and demographic scale enhance the ability to recover and mobilize resources. This observation is consistent with existing research on urban economic resilience [61]. Ecological and environmental indicators have a relatively limited but non-negligible influence. While the Green Space Ratio and Wastewater Coverage are generally performed worse across most regions, Hatay and Sanliurfa show slightly better performance, suggesting that ecological systems may play a supportive role in long-term recovery phases (Figure 8).

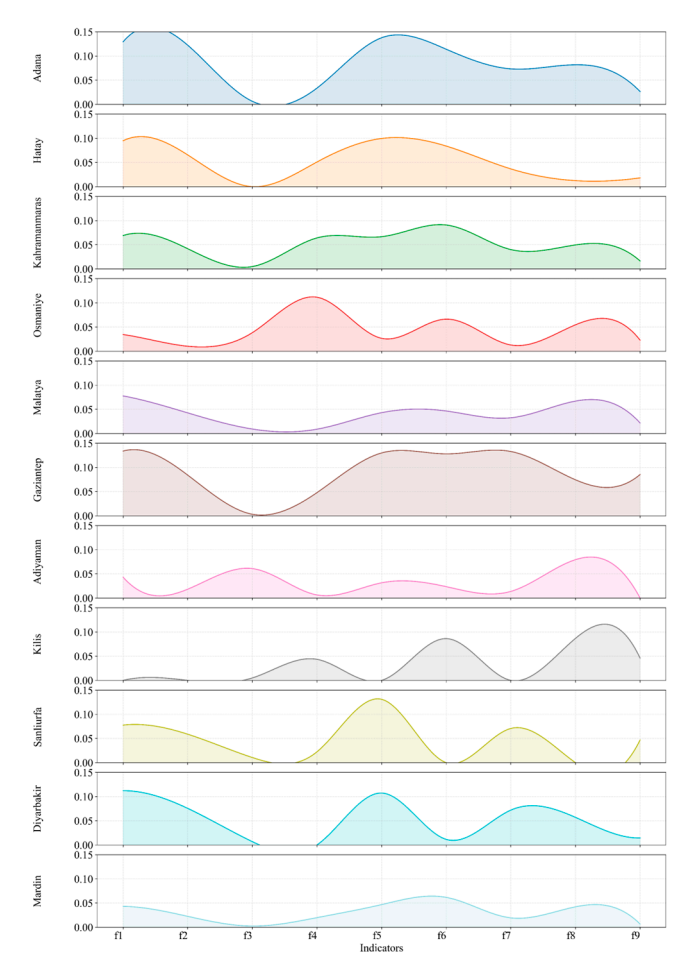


**Figure 8.** Contribution of each urban indicator to the urban earthquake RI. This figure presents the normalized contributions of nine indicators—including healthcare, infrastructure, socio-economic, and environmental variables—to the overall resilience of each region.

Urban earthquake resilience levels were further classified using the natural breakpoint method, and the regional distribution is visualized in Figure 9. Resilient regions are primarily located in the west and southwest, such as Adana, Osmaniye, and Gaziantep. Adana and Osmaniye, situated near the Mediterranean coast, exhibit stronger infrastructure and urban functionality, which contribute to higher resilience and recovery capacity. Vulnerable resilient regions are mainly found in central regions, including Kahramanmaras, Malatya, Adiyaman, and Sanliurfa, forming a transitional zone extending from west to east. Sluggish resilient regions, such as Hatay, Kilis, and Mardin, are primarily located in the southernmost and southeastern regions, exhibiting characteristics of spatial marginalization. These areas are often geographically remote, under-resourced, or constrained by various economic challenges, making them more vulnerable to seismic shocks. Specifically, Gaziantep, although located near the earthquake's epicenter, was classified as resilient, potentially due

Remote Sens. 2025, 17, 3431 15 of 22

to the region's strong economic base, urban scale, and post-disaster response capacity. This highlights the pivotal role of regional central regions in promoting post-disaster recovery.

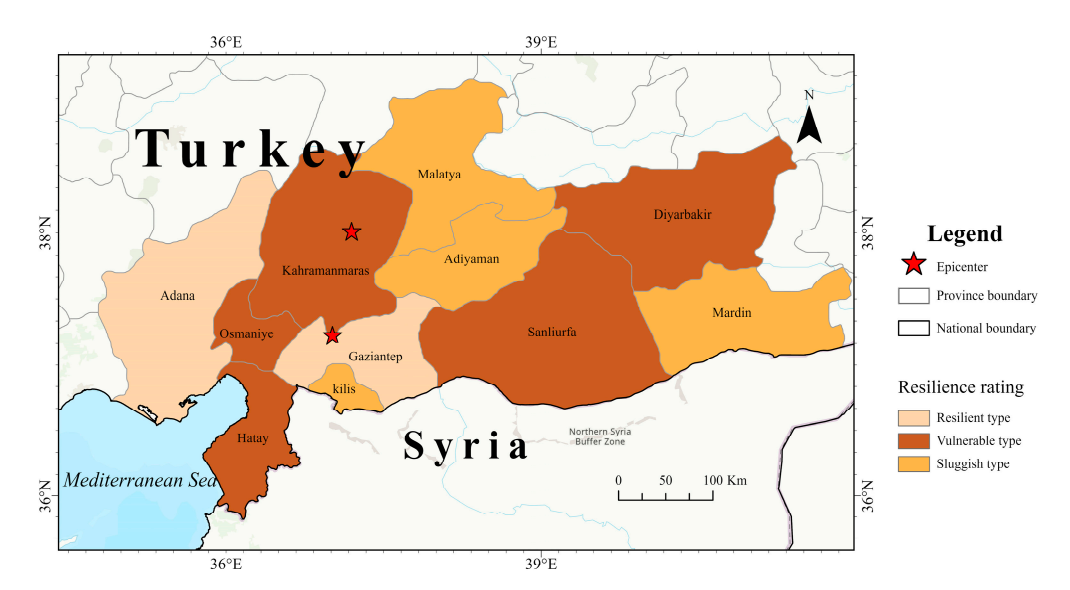


**Figure 9.** Graph of the spatial distribution of RI across the study area. Based on the RI, the eleven affected provinces are categorized into three levels: resilient, vulnerable, and sluggish types.

## 5. Discussion

#### 5.1. The Selection of the Method for Determining Weights

Rational weight assignment is essential for constructing a scientific urban resilience evaluation system. This study adopts the IG method, which demonstrates both practical effectiveness and theoretical soundness. For comparative analysis, the Entropy Weight Method and TOPSIS method are also applied, with results presented in Table 5.

Method	IG Method	TOPSIS Method	Entropy Weight Method
Total Number of Hospitals	0.1339	0.1218	0.0667
Total Number of Physicians	0.1223	0.1130	0.1020
Road Length	0.0610	0.0829	0.2408
Electricity Consumption	0.1117	0.1070	0.1247
Population	0.1378	0.1176	0.0842
Per Capita GDP	0.1281	0.1183	0.0854
Total Built-up Area	0.1330	0.1080	0.1183
Proportion of People Served by Wastewater Treatment	0.0869	0.1244	0.0620
Proportion of Green Space	0.0854	0.1070	0.1158

**Table 5.** Advantages of the IG method over the other two approaches.

From a practical perspective, the IG weights align well with the functional significance of each indicator. First, Population (0.1378) reflects the carrying capacity and organizational capacity of the urban social system. Although a larger population increases system complexity, it is often accompanied by stronger capabilities for resource allocation and mobilization, which form the foundation for long-term disaster resilience [62]. Second, medical resources, such as Total Number of Hospitals (0.1339) and Total Number of Physicians (0.1223), which are central to the public health emergencies, and their adequacy significantly influence urban resilience. Total Built-up Area (0.1330), as a representation of the region's physical infrastructure, reflects urban density and spatial structure, and also involves considerations of seismic design and structural safety [63]. Finally, Per Capita GDP (0.1281) reflects financial capacity for preparedness and recovery. It directly influences the efficiency of resource allocation and the speed of recovery.

Remote Sens. 2025, 17, 3431 16 of 22

From a theoretical standpoint, the IG method has clear advantages over conventional techniques. The entropy method emphasizes data variability, which may overvalue indicators with high fluctuation but low practical relevance, as seen in the excessive weight of f3 and the underestimation of key indicators like f1 and f8. Similarly, the TOPSIS method, which relies on Euclidean distance ranking, is significantly influenced by data distribution. For instance, the f8 indicator receives a disproportionately high weight that does not align with its actual significance. Both methods tend to exaggerate the importance of indicators with high variance but low practical relevance. In contrast, the IG method uses a hill-climbing algorithm to reveal causal relationships and quantify how much each indicator reduces decision uncertainty, representing a significant improvement over conventional techniques like the entropy method or TOPSIS that are often distorted by data variance [64] (in Figure 10).

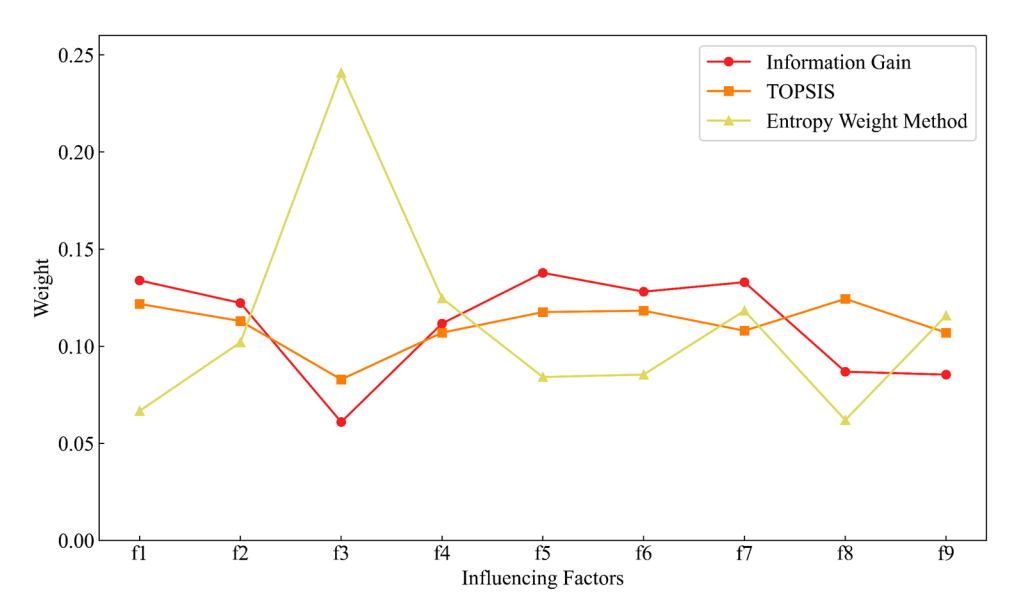


**Figure 10.** Comparison of three weight determination methods. This Figure compares the results of Information Gain (red line), TOPSIS (orange line), and the Entropy Weight Method (green line).

## 5.2. Analysis of the Differences Between CNLI and RI in Post-Earthquake Recovery Assessment

Urban resilience can be evaluated from multiple perspectives, and this study demonstrates that CNLI and RI capture distinct but complementary aspects of post-earthquake recovery. The RI is designed to reflect the intrinsic resilience level of a region. Urban resilience is considered an inherent and relatively stable attribute of a city, representing its systemic capacity to resist, absorb, and adapt to disturbances over time. It is not expected to fluctuate drastically in the short term [65]. As such, it remains relatively stable in the short term and indicates the potential for recovery prior to a disaster. In contrast, the CNLI, derived from NTL data, measures the real-time functional status of urban areas within a specific time window. It captures short-term fluctuations in activity levels and provides a dynamic, time-sensitive indicator of post-disaster operational performance.

The comparison of CNLI and RI reveals notable differences in regional recovery patterns. Taking Hatay, one of the most severely affected provinces, as an example, the earthquake triggered a fire at the port due to container collisions. International aid and reconstruction efforts have been continuously carried out after the earthquake. As a result, despite an initial drop in port activity, the overall NTL intensity of the port remained comparable to pre-earthquake levels. This can be attributed to sustained rescue operations, which required well-lit conditions throughout the week-long rescue and recovery period. According to high-resolution nighttime light imagery captured by Wuhan University's

Remote Sens. 2025, 17, 3431 17 of 22

"QMX-1" satellite on 18 February 2023 (in Figure 11), rescue activities were still intensively underway even after the fire was extinguished, and normal port functions were only partially restored several days later. These observations corroborate our analysis that emergency operations maintained elevated NTL levels, offsetting the post-disaster decline in regular economic activity. The NTL in this area recovered relatively quickly, with the CNLI value reaching the highest among the eleven study areas (0.88). However, the RI ranked only third, reflecting that Hatay possessed a moderate level of pre-disaster systemic recovery capacity. Conversely, Gaziantep, with the highest RI, also demonstrated strong CNLI performance, indicating both robust structural resilience and sustained functionality after the seismic shocks. Regions such as Mardin, with low RI and CNLI rankings, exemplify areas where weak inherent resilience aligns with poor post-disaster recovery, underscoring low potential for rapid restoration.

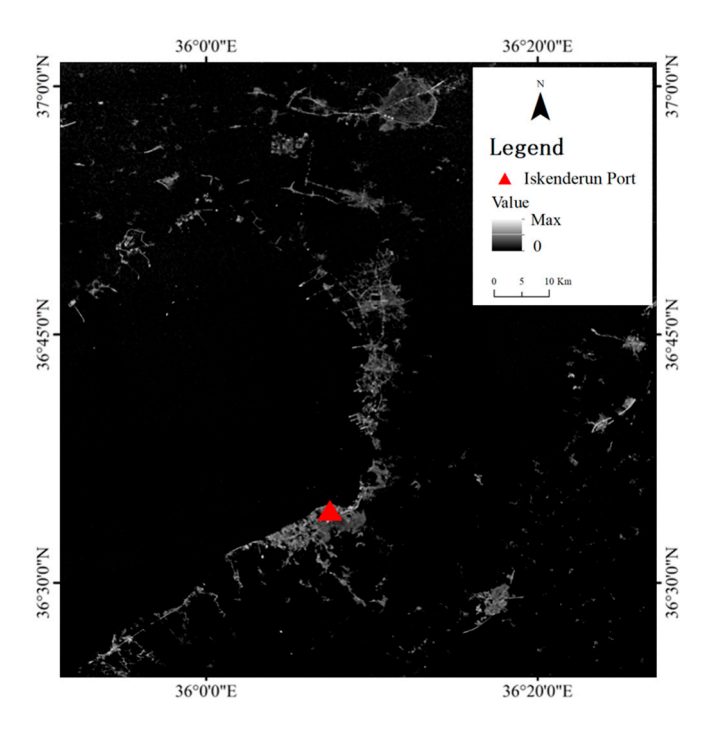


**Figure 11.** QMX-1 imagery acquired by Wuhan University on 18 February 2023, over the port area of Iskenderun, Turkey, showing post-earthquake conditions.

We also observed notable inconsistencies between CNLI and RI values in some regions. This discrepancy arises because CNLI and RI characterize two different aspects of urban systems: actual post-disaster recovery dynamics versus inherent resilience capacity. This dual-perspective framework analysis can take into account both the nighttime lighting performance of the region during the recovery period and the region's established basic capabilities. It is more comprehensive and interpretive than a single indicator, which is conducive to proposing differentiated regional recovery suggestions and improving recovery efficiency. To provide a more nuanced understanding, we proposed a dual-perspective framework that combines CNLI and RI to obtain integrated results (Figure 12).

Type I (high RI-high CNLI): Gaziantep, Adana, and Hatay. These regions demonstrate strong structural resilience and rapid NTL recovery, suggesting robust disaster response systems. They should be positioned as regional emergency hubs and further strengthen inter-regional coordination capacities [66].

Type II (high RI-low CNLI): Diyarbakir and Kaharamanmaras. Despite solid resilience foundations, their recovery lagged. Enhancing emergency management efficiency and promoting grassroots disaster preparedness are essential for improving response effectiveness [67].

Remote Sens. 2025, 17, 3431 18 of 22

Type III (low RI-high CNLI): Sanliurfa, Osmaniye, and Kilis. Although structurally less resilient, these regions showed strong post-disaster recovery momentum. Strengthening infrastructure and updating seismic design standards will help sustain recovery and build long-term resilience [68].

Type IV (low RI-low CNLI): Malatya and Adiyaman. Mardin, which is characterized by high vulnerability, requires prioritized support, including funding for reconstruction and service enhancement. Improving basic infrastructure and disaster preparedness will be key to advancing overall resilience capacity.

These findings indicate that RI and CNLI individually provide useful but incomplete pictures of post-disaster urban recovery. Integrating both indicators enables a more holistic assessment, supports refined regional classification, and informs targeted strategies to enhance earthquake resilience and recovery effectiveness.

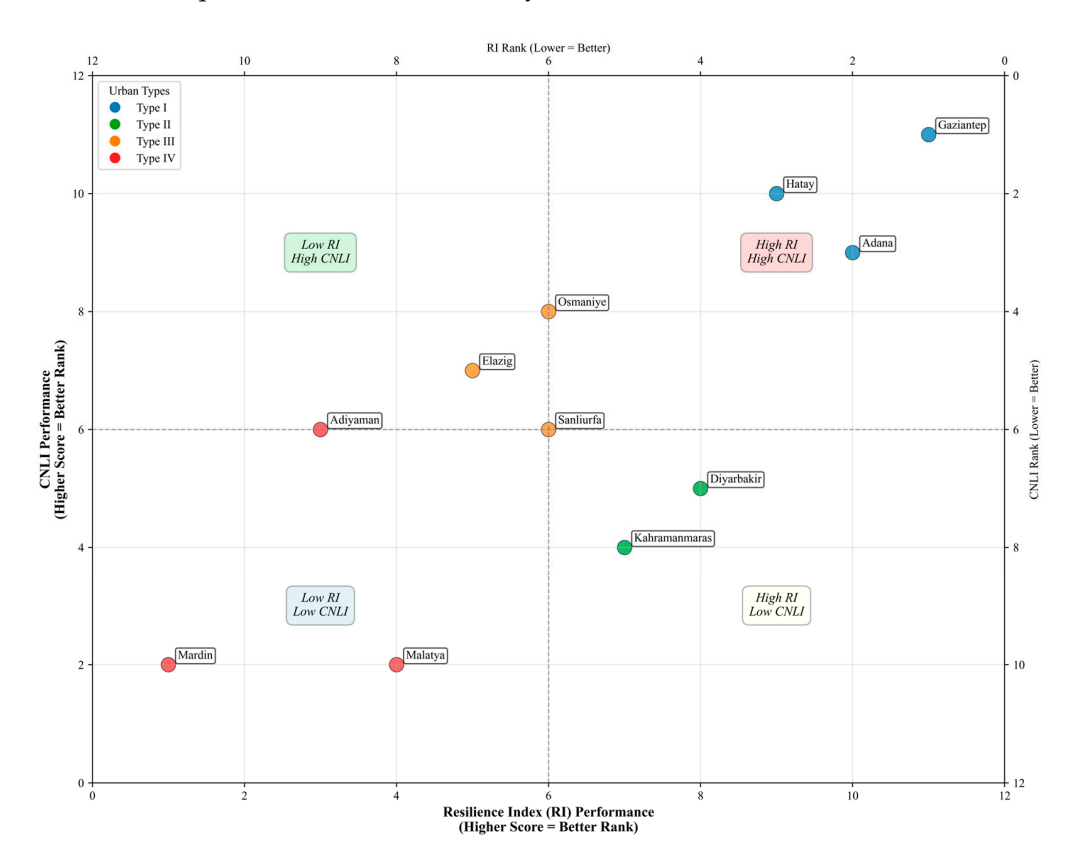


**Figure 12.** The comprehensive long-term post-earthquake evaluation results of CNLI and RI. Among them, CNLI reflects the recovery situation of the area after the earthquake, and RI reflects the inherent seismic resistance level within the area. The comprehensive analysis of the two leads to a new regional classification.

#### 5.3. Limitation

Although the 2023 Turkey-Syria earthquake was used for demonstration, if similar data is available, the proposed framework is generally applicable to assessing post-disaster damage and recovery in other regions. Due to limitations in the hierarchical distribution of statistical data, more comprehensive and fine-grained provincial-level data for assessment modeling are currently unavailable, which may simplify the complexity and nuances of urban resilience. Urban resilience is inherently multidimensional, encompassing aspects such as governance, community participation, and cultural factors. Future studies will incorporate additional indicators into resilience model calculations to provide a deeper understanding of what urban resilience entails, thereby enhancing both practicality and accuracy. Furthermore, although the use of NPP/VIIRS NTL data facilitates quantitative

Remote Sens. 2025, 17, 3431

assessment of damage and recovery post-earthquake impacts, higher-resolution NTL data (such as those from SDGSAT-1) would better capture intra-urban NTL details, particularly in smaller regions. Due to resolution limitations, the analysis primarily focuses on urban and densely populated areas, making it difficult to accurately assess small, scattered rural settlements along fault zones. Finally, expand the analysis to other types of disasters to verify the universality of the framework. Additionally, introducing more influential indicators can deepen our understanding of urban resilience.

#### 6. Conclusions

This study explores the use of NTL data for post-earthquake damage and recovery assessment at a regional scale. For damage assessment, pixel-level indicators are introduced for auxiliary analysis, which are four quantitative indicators (TNTL, NNTL, NLL, ARR) employed to identify the most severely affected areas. Hatay exhibited the highest values of NLL and ARR (28.8% and 41.73%, respectively), indicating both severe intensity and spatial extent of damage. Compared with traditional TNTL-based assessments, the addition of auxiliary indicators enabled a more comprehensive evaluation of seismic impacts.

For recovery assessment, we integrated four key indicators, DS, RS, PSS, and EIC, to construct CNLI. This index provides a large-scale, rapid measure of human activity during the recovery period. Results suggest that Hatay, Gaziantep, and Kilis demonstrated stronger recovery performance, whereas Kahramanmaras, Mardin, and Malatya lagged behind. To further investigate the underlying drivers of these patterns, we developed a regional RI based on statistical indicators and land-use data. By modeling the complex interdependencies among variables with a Bayesian Network, we captured cross-dimensional relationships often overlooked by conventional methods. Moreover, an IG-based approach was applied to quantify the contribution of each indicator to the reduction in recovery uncertainty. The results indicate that Gaziantep and Adana display high resilience capacity, while Malatya, Adiyaman, Kilis, and Mardin exhibit weaker resilience. We also observed notable inconsistencies between CNLI and RI values in some regions. Combining both indices allows for a more holistic assessment of regional performance, which we further classified into four types to provide targeted and explainable recovery recommendations.

The proposed framework contributes to more informed post-disaster decision-making and encourages a strategic shift from passive recovery to proactive risk reduction. It provides scientific support for earthquake emergency response and efficient reconstruction.

**Author Contributions:** Conceptualization, J.Y.; methodology, J.Y. and Z.W.; software, Y.S. and Y.Z.; validation, Z.W., J.Z. and M.W.; investigation, A.Z. and Q.L.; writing—original draft preparation, J.Y.; writing—review and editing, S.C. and Z.W.; supervision, S.C.; project administration, S.C.; funding acquisition, S.C. All authors have read and agreed to the published version of the manuscript.

**Funding:** This research was funded by the National Key Research and Development Program of China (grant No. 2020YFA0714103).

Data Availability Statement: The data presented in this study are openly available in Monthly NPP/VIIRS Night-time Light Data at <a href="https://eogdata.mines.edu/products/vnl/">https://eogdata.mines.edu/products/vnl/</a>, accessed on 2 December 2024; Daily NPP/VIIRS VNP46A2 data at <a href="https://ladsweb.modaps.eosdis.nasa.gov/">https://ladsweb.modaps.eosdis.nasa.gov/</a>, accessed on 5 December 2024; Land cover Data at <a href="https://livingatlas.arcgis.com/landcoverexplorer">https://livingatlas.arcgis.com/landcoverexplorer</a>, accessed on 24 December 2024; Global Administrative Areas database (GADM) at <a href="https://www.gadm.org/">https://www.gadm.org/</a>, accessed on 4 February 2025; QMX-1 data at <a href="https://qmx.whu.edu.cn/sjfw.htm">https://www.gadm.org/</a>, accessed on 4 February 2025; QMX-1 data at <a href="https://www.tuik.gov.tr/Home/Index">https://www.tuik.gov.tr/Home/Index</a>, accessed on 25 September 2025; and epicentral coordinate at <a href="https://earthquake.usgs.gov/earthquakes/map/">https://earthquake.usgs.gov/earthquakes/map/</a>, accessed on 25 September 2025. In addition, the raw data supporting the conclusions of this article will be made available by the authors on request.

Remote Sens. 2025, 17, 3431 20 of 22

**Acknowledgments:** Acknowledgement for the data support from the NASA and the Earth Observation Group for providing the Nighttime light Data. The authors also thank the anonymous reviewers and the editors for their insightful comments and helpful suggestions to improve our manuscript.

**Conflicts of Interest:** The authors declare no conflicts of interest.

#### References

- 1. Mannakkara, S.; Wilkinson, S.; Potangaroa, R. Resilient Post Disaster Recovery Through Building Back Better; Routledge: Oxfordshire, UK, 2018.
- 2. Cutter, S.L.; Burton, C.G.; Emrich, C.T. Disaster resilience indicators for benchmarking baseline conditions. *J. Homel. Secur. Emerg. Manag.* **2010**, 7, 1–24. [CrossRef]
- Kondraganti, A. Big Data Analytics in Humanitarian and Disaster Operations: A Systematic Review. arXiv 2021, arXiv:2108.09800.
   [CrossRef]
- February 2024 Issue Campaign: Disaster Relief. Available online: https://globalwa.org/2024/02/february-2024-issue-campaign-disaster-relief/ (accessed on 16 December 2024).
- 5. Hariri-Ardebili, M.A.; Speicher, M.S. Reconnaissance-informed post-earthquake functional recovery: Observations and challenges. *Earthq. Spectra* **2025**, *41*, 88–125. [CrossRef]
- 6. Fotouhi, A.; Qiang, H.; Ding, M.; Hassan, M.; Giordano, L.G.; Garcia-Rodriguez, A.; Yuan, J. Survey on UAV Cellular Communications: Practical Aspects, Standardization Advancements, Regulation, and Security Challenges. *IEEE Commun. Surv. Tutor.* 2019, 21, 3417–3442. [CrossRef]
- 7. Kizilay, F.; Narman, M.R.; Song, H.; Narman, H.S.; Cosgun, C.; Alzarrad, A. Evaluating fine tuned deep learning models for real-time earthquake damage assessment with drone-based images. *Al Civ. Eng.* **2024**, *3*, 15. [CrossRef]
- 8. Levin, N.; Kyba, C.C.; Zhang, Q.; de Miguel, A.S.; Román, M.O.; Li, X.; Portnov, B.A.; Molthan, A.L.; Jechow, A.; Miller, S.D. Remote sensing of night lights: A review and an outlook for the future. *Remote Sens. Environ.* **2020**, 237, 111443. [CrossRef]
- 9. Yu, M.; Guo, S.; Guan, Y.; Cai, D.; Zhang, C.; Fraedrich, K.; Liao, Z.; Zhang, X.; Tian, Z. Spatiotemporal heterogeneity analysis of Yangtze River Delta urban agglomeration: Evidence from nighttime light data (2001–2019). *Remote Sens.* **2021**, *13*, 1235. [CrossRef]
- 10. Levin, N.; Kyba, C.C.M.; Zhang, Q. Remote Sensing of Night Lights—Beyond DMSP. Remote Sens. 2019, 11, 1472. [CrossRef]
- 11. Li, F.; Wang, Q.; Hu, W.; Liu, J.; Zhang, X. Rapid assessment of disaster damage and economic resilience in relation to the flooding in Zhengzhou, China in 2021. *Remote Sens. Lett.* **2022**, *13*, 651–662. [CrossRef]
- 12. Yuan, Y.; Wang, C.; Liu, S.; Chen, Z.; Ma, X.; Li, W.; Zhang, L.; Yu, B. The changes in nighttime lights caused by the Turkey–Syria earthquake using NOAA-20 VIIRS day/night band data. *Remote Sens.* **2023**, *15*, 3438. [CrossRef]
- 13. Kohiyama, M.; Hayashi, H.; Maki, N.; Higashida, M.; Kroehl, H.; Elvidge, C.; Hobson, V. Early damaged area estimation system using DMSP-OLS night-time imagery. *Int. J. Remote Sens.* **2004**, *25*, 2015–2036. [CrossRef]
- 14. Liu, Z.; Zhang, J.; Li, X.; Chen, X. Long-term resilience curve analysis of wenchuan earthquake-affected counties using dmsp-ols nighttime light images. *IEEE J. Sel. Top. Appl. Earth Obs. Remote Sens.* **2021**, *14*, 10854–10874. [CrossRef]
- 15. Zhao, X.; Yu, B.; Liu, Y.; Yao, S.; Lian, T.; Chen, L.; Yang, C.; Chen, Z.; Wu, J. NPP-VIIRS DNB daily data in natural disaster assessment: Evidence from selected case studies. *Remote Sens.* **2018**, *10*, 1526. [CrossRef]
- 16. Fan, X.; Nie, G.; Deng, Y.; An, J.; Zhou, J.; Li, H. Rapid detection of earthquake damage areas using VIIRS nearly constant contrast night-time light data. *Int. J. Remote Sens.* **2019**, *40*, 2386–2409.
- 17. Xiao, Z.; Pan, Y.; Jiang, L.; Wang, Z.; Shi, K. Remote Sensing Nighttime Lights Reveal the Post-Earthquake Losses and Reconstruction Situations in Turkey–Syria Earthquake Areas. *IEEE Geosci. Remote Sens. Lett.* **2024**, *21*, 1–5. [CrossRef]
- 18. Yu, B.; Chen, F.; Wang, N.; Wang, L.; Guo, H. Assessing changes in nighttime lighting in the aftermath of the Turkey-Syria earthquake using SDGSAT-1 satellite data. *Innovation* **2023**, *4*, 100419.
- 19. Li, X.; Cao, H.; Gong, Y. Turkey-Syria Earthquake Assessment Using High-Resolution Night-time Light Images. *Geomat. Inf. Sci. Wuhan Univ.* **2023**, 48, 1697–1705.
- Li, X.; Liu, A.; Zhu, R.; Zhang, X. Identification of Qinghai Menyuan Ms6. 9 earthquake-stricken area based on VNP46A2 night lighting image. In Proceedings of the Second International Conference on Geographic Information and Remote Sensing Technology (GIRST 2023), Qingdao, China, 21–23 July 2023; pp. 156–161.
- 21. Martinez, J.F.; MacManus, K.; Stokes, E.C.; Wang, Z.; de Sherbinin, A. Suitability of nasa's black marble daily nighttime lights for population studies at varying spatial and temporal scales. *Remote Sens.* **2023**, *15*, 2611. [CrossRef]
- 22. Islam, K.S. Utilizing Nasa's Black Marble to Measure the Change in Electrification and Regional Inequality of Dhaka, Bangladesh. Master's Thesis, Binghamton University, Binghamton, NY, USA, 2023.
- 23. Tveit, T.; Skoufias, E.; Strobl, E. Using VIIRS nightlights to estimate the impact of the 2015 Nepal earthquakes. *Geoenviron. Disasters* **2022**, *9*, 2. [CrossRef]

Remote Sens. 2025, 17, 3431 21 of 22

24. Supporting Disaster Assessment and Response with the VIIRS Day-Night Band. Available online: https://ntrs.nasa.gov/citations/20150002880 (accessed on 12 December 2024).

- 25. Li, X.; Zhan, C.; Tao, J.; Li, L. Long-term monitoring of the impacts of disaster on human activity using DMSP/OLS nighttime light data: A case study of the 2008 Wenchuan, China Earthquake. *Remote Sens.* **2018**, *10*, 588. [CrossRef]
- 26. Wang, J.; Zhang, J.; Gong, L.; Li, Q.; Zhou, D. Indirect seismic economic loss assessment and recovery evaluation using nighttime light images–application for Wenchuan earthquake. *Nat. Hazards Earth Syst. Sci.* **2018**, *18*, 3253–3266. [CrossRef]
- 27. Gao, S.; Chen, Y.; Liang, L.; Gong, A. Post-earthquake night-time light piecewise (PNLP) pattern based on NPP/VIIRS night-time light data: A case study of the 2015 Nepal earthquake. *Remote Sens.* **2020**, *12*, 2009. [CrossRef]
- 28. Barton-Henry, K.; Wenz, L. Nighttime light data reveal lack of full recovery after hurricanes in Southern US. *Environ. Res. Lett.* **2022**, *17*, 114015. [CrossRef]
- 29. Saja, A.A.; Goonetilleke, A.; Teo, M.; Ziyath, A.M. A critical review of social resilience assessment frameworks in disaster management. *Int. J. Disaster Risk Reduct.* **2019**, *35*, 101096. [CrossRef]
- 30. Berkes, F.; Ross, H. Panarchy and community resilience: Sustainability science and policy implications. *Environ. Sci. Policy* **2016**, 61, 185–193. [CrossRef]
- 31. Bhamra, R.; Dani, S.; Burnard, K. Resilience: The concept, a literature review and future directions. *Int. J. Prod. Res.* **2011**, *49*, 5375–5393. [CrossRef]
- 32. Klein, R.J.; Nicholls, R.J.; Thomalla, F. Resilience to natural hazards: How useful is this concept? *Glob. Environ. Change Part B Environ. Hazards* **2003**, *5*, 35–45. [CrossRef]
- 33. Liu, W.; Zhou, J.; Li, X.; Zheng, H.; Liu, Y. Urban resilience assessment and its spatial correlation from the multidimensional perspective: A case study of four provinces in North-South Seismic Belt, China. *Sustain. Cities Soc.* **2024**, *101*, 105109. [CrossRef]
- 34. Xu, H.; Li, Y.; Tan, Y.; Deng, N. A scientometric review of urban disaster resilience research. *Int. J. Environ. Res. Public Health* **2021**, 18, 3677. [CrossRef]
- 35. Zhao, R.; Fang, C.; Liu, H. Progress and prospect of urban resilience research. Prog. Geogr. 2020, 39, 1717–1731. [CrossRef]
- 36. Liu, Z.; Ma, R. Construction and Application of an Urban Resilience Evaluation System from the Perspective of Disaster Prevention and Mitigation—A Study of 13 Cities in Jiangsu Province. *J. China Emerg. Manag. Sci.* **2021**, 27–41. [CrossRef]
- 37. Xiaojing, M.; Xin, C.; Jiajing, C.; Honggang, Y. Application of Combination Weighting and TOPSIS in Urban Regional Resilience Assessment under Flood Disaster. *Safe Environ.* **2023**, *23*, 1465–1473. [CrossRef]
- 38. Xu, W.; Yu, Q.; Proverbs, D. Evaluation of factors found to influence urban flood resilience in China. *Water* **2023**, *15*, 1887. [CrossRef]
- 39. Ma, M.; Zhang, Y.; Zhang, J.; Li, M.; Zhu, J.; Wang, Y. Assessment of urban seismic social vulnerability based on game theory combination and TOPSIS model: A case study of Changchun City. *Sci. Rep.* **2025**, *15*, 8189. [CrossRef]
- 40. Tarakçi, E.; Eti, S.; Can, E. Integrated Spherical Fuzzy-CRITIC and Spherical Fuzzy-TOPSIS Method in Prioritizing Earthquake Risks and Planning: An Overview in Disaster Management. In Proceedings of the International Conference on Intelligent and Fuzzy Systems, Canakkale, Türkiye, 16–18 July 2024; pp. 649–657.
- 41. Zhu, J.; Zhang, Y.; Zhang, J.; Chen, Y.; Liu, Y.; Liu, H. Multi-criteria seismic risk assessment based on combined weight-TOPSIS model and CF-logistic regression model—A case study of Songyuan City, China. *Sustainability* **2023**, *15*, 11216. [CrossRef]
- 42. Alemdar, K.D. Seismic risk assessment of transportation networks for the impending Istanbul earthquake with GIS-based MCDM approach. *Nat. Hazard.* **2025**, *121*, 10085–10123. [CrossRef]
- 43. Meshkini, A.; Alipour, S. Analysis of the social resilience of housing in urban areas against earthquakes: The case study of areas of the 15th district of Tehran. *Geogr. Urban Plan. Res.* (GUPR) **2024**, 12, 1–22.
- 44. Zakeri, S.; Konstantas, D.; Chatterjee, P.; Zavadskas, E.K. Soft cluster-rectangle method for eliciting criteria weights in multi-criteria decision-making. *Sci. Rep.* **2025**, *15*, 284. [CrossRef]
- 45. Bánhidi, Z.; Dobos, I. Sensitivity of TOPSIS ranks to data normalization and objective weights on the example of digital development. *Cent. Eur. Oper. Res.* **2024**, 32, 29–44. [CrossRef]
- 46. Agarwal, R.; Melnick, L.; Frosst, N.; Zhang, X.; Lengerich, B.; Caruana, R.; Hinton, G.E. Neural additive models: Interpretable machine learning with neural nets. *Adv. Neural Inf. Process. Syst.* **2021**, *34*, 4699–4711.
- 47. Garbero, A.; Letta, M. Predicting household resilience with machine learning: Preliminary cross-country tests. *Empir. Econ.* **2022**, 63, 2057–2070. [CrossRef]
- 48. Ren, C.; Wang, Z.; Taymaz, T.; Hu, N.; Luo, H.; Zhao, Z.; Yue, H.; Song, X.; Shen, Z.; Xu, H.; et al. Supershear triggering and cascading fault ruptures of the 2023 Kahramanmaraş, Türkiye, earthquake doublet. *Science* **2024**, *383*, 305–311. [CrossRef]
- 49. Işık, E.; Avcil, F.; Büyüksaraç, A.; İzol, R.; Hakan Arslan, M.; Aksoylu, C.; Harirchian, E.; Eyisüren, O.; Arkan, E.; Şakir Güngür, M.; et al. Structural damages in masonry buildings in Adıyaman during the Kahramanmaraş (Turkiye) earthquakes (Mw 7.7 and Mw 7.6) on 06 February 2023. *Eng. Fail. Anal.* 2023, 151, 107405. [CrossRef]

Remote Sens. 2025, 17, 3431 22 of 22

50. Liang, P.; Xu, Y.; Zhou, X.; Li, Y.; Tian, Q.; Zhang, H.; Ren, Z.; Yu, J.; Li, C.; Gong, Z.; et al. Coseismic surface ruptures of MW7.8 and MW7.5 earthquakes occurred on February 6, 2023, and seismic hazard assessment of the East Anatolian Fault Zone, Southeastern Türkiye. *Sci. China Earth Sci.* 2025, 68, 611–625.

- 51. Román, M.O.; Wang, Z.; Sun, Q.; Kalb, V.; Miller, S.D.; Molthan, A.; Schultz, L.; Bell, J.; Stokes, E.C.; Pandey, B. NASA's Black Marble nighttime lights product suite. *Remote Sens. Environ.* **2018**, 210, 113–143.
- 52. Elvidge, C.D.; Baugh, K.E.; Zhizhin, M.; Hsu, F.-C. Why VIIRS data are superior to DMSP for mapping nighttime lights. *Proc. Asia-Pac. Adv. Netw.* **2013**, *35*, 62–69. [CrossRef]
- 53. VNP46A2: VIIRS Lunar Gap-Filled BRDF Nighttime Lights Daily L3 Global 500m. Available online: https://developers.google.com/earth-engine/datasets/catalog/NASA\_VIIRS\_002\_VNP46A2?hl=zh-cn (accessed on 8 August 2024).
- 54. Zhao, M.; Zhou, Y.; Li, X.; Cao, W.; He, C.; Yu, B.; Li, X.; Elvidge, C.D.; Cheng, W.; Zhou, C. Applications of Satellite Remote Sensing of Nighttime Light Observations: Advances, Challenges, and Perspectives. *Remote Sens.* **2019**, *11*, 1971.
- 55. Yavas, C.E.; Chen, L.; Kadlec, C.; Ji, Y. Improving earthquake prediction accuracy in Los Angeles with machine learning. *Sci. Rep.* **2024**, *14*, 24440. [CrossRef]
- 56. Heckerman, D.; Geiger, D.; Chickering, D.M. Learning Bayesian networks: The combination of knowledge and statistical data. *Mach. Learn.* **1995**, *20*, 197–243. [CrossRef]
- 57. Martínez-Morales, M.; Cruz-Ramírez, N.; Jiménez-Andrade, J.L.; Garza-Domínguez, R. Bayes-N: An Algorithm for Learning Bayesian Networks from Data Using Local Measures of Information Gain Applied to Classification Problems. In Proceedings of the MICAI 2004: Advances in Artificial Intelligence, Mexico City, Mexico, 26–30 April 2004; pp. 527–535.
- 58. Global Rapid Post-Disaster Damage Estimation (GRADE) Report: February 6, 2023 Kahramanmaraş Earthquakes-Türkiye Report (English). Available online: https://documents.worldbank.org/en/publication/documents-reports/documentdetail/099022 723021250141/p1788430aeb62f08009b2302bd4074030fb (accessed on 1 October 2024).
- 59. Kawase, H. The Cause of the Damage Belt in Kobe: "The Basin-Edge Effect," Constructive Interference of the Direct S-Wave with the Basin-Induced Diffracted/Rayleigh Waves. *Seismol. Res. Lett.* **1996**, *67*, 25–34. [CrossRef]
- 60. Nipa, T.J.; Kermanshachi, S.; Pamidimukkala, A. Identification of Resilience Dimensions in Critical Transportation Infrastructure Networks. J. Leg. Aff. Disput. Resolut. Eng. Constr. 2023, 15, 03122001. [CrossRef]
- 61. García, I. Beyond Urban-centered responses: Overcoming challenges to build disaster resilience and long-term sustainability in rural areas. *Sustainability* **2024**, *16*, 4373. [CrossRef]
- 62. Yabe, T.; Rao, P.S.C.; Ukkusuri, S.V. Resilience of interdependent urban socio-physical systems using large-scale mobility data: Modeling recovery dynamics. *Sustain. Cities Soc.* **2021**, 75, 103237. [CrossRef]
- 63. Qin, R.; Cui, P.; Zhou, S.; Zhang, F. Dynamic Analysis for Enhancing Urban Resilience Against Public Health Emergencies of International Concern. *Land* **2024**, *13*, 2220. [CrossRef]
- 64. Kaya, R.; Salhi, S.; Spiegler, V. A novel integration of MCDM methods and Bayesian networks: The case of incomplete expert knowledge. *Ann. Oper. Res.* **2023**, *320*, 205–234. [CrossRef]
- 65. Taylor, P.J.; Hoyler, M.; Verbruggen, R. External urban relational process: Introducing central flow theory to complement central place theory. *Urban Stud.* **2010**, *47*, 2803–2818. [CrossRef]
- 66. Wang, J.; Deng, Y.; Kumari, S.; Song, Z. Research on the Spatial Spillover Effect of Transportation Infrastructure on Urban Resilience in Three Major Urban Agglomerations in China. *Sustainability* **2023**, *15*, 5543. [CrossRef]
- 67. The Ten Essentials for Making Cities Resilient. Available online: https://mcr2030.undrr.org/ten-essentials-making-cities-resilient (accessed on 2 February 2025).
- 68. Ma, C.; Qirui, C.; Lv, Y. "One community at a time": Promoting community resilience in the face of natural hazards and public health challenges. *BMC Public Health* **2023**, 23, 2510. [CrossRef]

**Disclaimer/Publisher's Note:** The statements, opinions and data contained in all publications are solely those of the individual author(s) and contributor(s) and not of MDPI and/or the editor(s). MDPI and/or the editor(s) disclaim responsibility for any injury to people or property resulting from any ideas, methods, instructions or products referred to in the content.